

Article

Morphological Evolution of La_2NiO_4 Coatings Synthesized by Reactive Magnetron Sputtering (RMS) at High Pressure as Cathode for Intermediate Temperature Solid Oxide Fuel Cell (IT-SOFC)

Xiaolei Ye ^{1,2}, Huan Luo ^{3,*}, Ming Hou ^{4,*}, Pierre Bertrand ⁵, Alain Billard ^{1,2}  and Pascal Briois ^{1,2} 

¹ FEMTO-ST Institute (UMR CNRS 6174), UBFC/UTBM, Site de Montbéliard, F-90010 Belfort, France; xiaolei.ye@utbm.fr (X.Y.); alain.billard@utbm.fr (A.B.); pascal.briois@utbm.fr (P.B.)

² USR FC Lab (CNRS FR3539), F-90010 Belfort, France

³ School of Materials Science and Engineering, Xi'an University of Science and Technology, Xi'an 710054, China

⁴ Faculty of Metallurgical and Energy Engineering, Kunming University of Science and Technology, Kunming 650093, China

⁵ ICB (UMR CNRS 6303), UBFC/UTBM, Site de Sévenans, F-90010 Belfort, France; pierre.bertrand@utbm.fr

* Correspondence: luohuan@xust.edu.cn (H.L.); houmingkmust@163.com (M.H.)

Abstract: This work focuses on the evolution of the morphology and structure of La_2NiO_4 (namely, LNO) coatings deposited by reactive magnetron sputtering (RMS) with subsequent annealing processes. The LNO coatings start to crystallize at 600 °C, and the LNO with K_2NiF_4 structure was formed at 700 °C. A small amount of $\text{La}_3\text{Ni}_2\text{O}_7$ appeared in the La_2NiO_4 coatings at 1100 °C. Interestingly, the LNO coatings realize the transformation from dense to different porous morphologies due to the annealing process. The LNO coating with abundant pores was formed after annealing treatment at 1000 °C for 2 h. This porous morphology can be stably maintained after short-term thermal stability experiments at 750 °C for 120 h. The electrochemical impedance spectroscopy (EIS) measurement of the LNO/YSZ/LNO symmetrical half-cells shows that the LNO cathode coating after annealing at 1000 °C for 2 h exhibits lower polarization resistance (R_{pol}) and activation energy.

Keywords: reactive magnetron sputtering; annealing; morphological evolution; electrochemical impedance spectroscopy; IT-SOFC



Citation: Ye, X.; Luo, H.; Hou, M.; Bertrand, P.; Billard, A.; Briois, P. Morphological Evolution of La_2NiO_4 Coatings Synthesized by Reactive Magnetron Sputtering (RMS) at High Pressure as Cathode for Intermediate Temperature Solid Oxide Fuel Cell (IT-SOFC). *Coatings* **2023**, *13*, 1113. <https://doi.org/10.3390/coatings13061113>

Academic Editor: Dimitrios Tasis

Received: 30 May 2023

Revised: 13 June 2023

Accepted: 15 June 2023

Published: 16 June 2023



Copyright: © 2023 by the authors. Licensee MDPI, Basel, Switzerland. This article is an open access article distributed under the terms and conditions of the Creative Commons Attribution (CC BY) license (<https://creativecommons.org/licenses/by/4.0/>).

1. Introduction

As an energy conversion device, the solid oxide fuel cell (SOFC) can directly convert chemical energy into electrical energy. However, the SOFC working in the high temperature range of 800–1000 °C causes high cost in materials and challenges in compatibility [1]. The last generation of solid oxide fuel cells operating at intermediate temperatures (IT, 500–750 °C) can alleviate these drawbacks and increase the cell lifetime [2]. However, the low operating temperature leads to the catalytic activity for the oxygen reduction reaction (ORR), which in turn degrades the cell performance. To address this issue, considerable efforts have been devoted to developing novel materials with enhanced ORR performance [3–5]. Some materials such as $\text{La}_{1-x}\text{Sr}_x\text{Co}_{1-y}\text{Fe}_y\text{O}_{3-\delta}$ (LSCF), $\text{La}_{0.6}\text{Sr}_{0.4}\text{CoO}_{3-\delta}$ (LSC), $\text{La}_{0.8}\text{Sr}_{0.2}\text{MnO}_3$ (LSM), $\text{Sm}_{0.5}\text{Sr}_{0.5}\text{CoO}_{3-\delta}$ (SSC), or $\text{Ba}_{0.5}\text{Sr}_{0.5}\text{Co}_{0.8}\text{Fe}_{0.2}\text{O}_{3-\delta}$ (BSCF) have been proposed as the cathode [6–8]. Unfortunately, these cathode materials were still not perfect for practical applications, mainly due to insufficient ORR activity or stability, and/or incompatibility with other cell components (electrolyte or interconnectors). On the other hand, in attempts to find new materials that can be used as cathodes for IT-SOFC, a class of perovskite-type materials with K_2NiF_4 structure has received more attention due to their mixed ionic and electronic conductivity (MIEC) [9]. La_2NiO_4 is a typical K_2NiF_4 -type material that exhibits excellent performance on surface oxygen exchange and chemical

stability from room temperature up to 1300 °C [10,11]. In addition, the thermal expansion coefficient of La_2NiO_4 ($13.0 \times 10^{-6} \text{ K}^{-1}$) is close to that of the commonly used electrolyte yttria stabilized zirconia (YSZ, $11.6 \times 10^{-6} \text{ K}^{-1}$) and ferritic steel interconnect materials ($11.0\text{--}12.5 \times 10^{-6} \text{ K}^{-1}$) [12,13]. The application of La_2NiO_4 to half cells and single cells with different electrolytes has been studied and has shown interesting results. The R_p of La_2NiO_4 in a symmetrical cell configuration are $5.2 \Omega \cdot \text{cm}^2$ [14] and $2.2 \Omega \cdot \text{cm}^2$ [15] at 600 °C in air, which is much lower than $72.54 \Omega \cdot \text{cm}^2$ for $\text{La}_{0.8}\text{Sr}_{0.2}\text{MnO}_3$ (LSM) [16].

Physical vapor deposition techniques are widely used to deposit dense electrolyte layers [17] or barrier layers [18] in the field of SOFC. Recently, cathode coatings deposited by this technique have also gained attention [19,20]. Previous work in our laboratory has demonstrated that Ln_2NiO_4 ($\text{Ln} = \text{La}, \text{Pr}, \text{Nd}$) coatings as the cathode on the half-cell and/or single cell can be successfully synthesized by RMS with promising results [10,20,21]. However, the morphology evolution of the coatings deposited by magnetron sputtering deserves further investigation in order to obtain suitable porous structures. This is helpful to further promote the application of magnetron sputtering in SOFC cathode preparation.

This work focuses mainly on the exploration of the synthesis of a porous LNO cathode by RMS. The evolution of the morphology and structure of the LNO coating was investigated as a function of the annealing treatment temperature. The electrochemical performance of LNO cathodes with different morphologies was evaluated by measuring the electrochemical impedance spectroscopy of LNO/YSZ/LNO symmetric cells. The link between the electrochemical performance and morphology of LNO cathodes deposited by magnetron sputtering is demonstrated. This work can provide a reliable reference for the synthesis of porous SOFC cathode layers by magnetron sputtering.

2. Experimental Procedure

2.1. Deposition Device

The DC reactive magnetron sputtering technique was used to synthesize La_2NiO_4 material by using metallic La and Ni targets with a purity of 99.9% ($\phi 145 \times 6$ mm) in a mixture atmosphere of argon and oxygen. A 90 L sputtering chamber vacuumed by a turbo molecular pump allowing less than 10^{-5} Pa as the base vacuum was used. The argon and oxygen flow rates were controlled by using Brooks flowmeters, and the total pressure measurement was performed via an MKS Baratron gauge. The substrates were positioned on a substrate holder at the draw distance of 70 mm parallel to the sources and rotated to ensure a homogenous deposition. The targets mounted on the unbalanced magnetron were powered through pulsed DC generators allowing the power discharge control. Alumina ceramic and yttria stabilized zirconia (YSZ) pellets as well as glass slides were used as substrate supporting coating to measure various properties such as structure, conductivity, chemical composition, electrical properties, and optical transmittance. All substrates were cleaned with alcohol and soap, and then rinsed with water and dried prior to deposition.

2.2. Characterization

The morphology and composition of the coatings were characterized by scanning electron microscopy (SEM) equipped with energy dispersive spectroscopy (EDS) via a JEOL JSM 5800 LV. The pore size distribution of the coating was obtained from the SEM results by using Nano Measurer 1.2. The structure of the coatings was determined by X-ray diffraction (XRD, BRUKER D8) with $\text{Co-K}_{\alpha 1+\alpha 2}$ at 35 kV and 40 mA. The diffraction patterns were collected at room temperature in the angle range of $20^\circ \leq 2\theta \leq 90^\circ$ with a scan step of 0.019° . The thickness of the coatings was measured using an Altysurf profilometer allowing an accuracy of about 20 nm. A UV-visible-NIR Shimadzu VU-3600 spectrophotometer controlled by UV probe 2.33 software was used to measure the optical transmittance of the coatings deposited on the glass substrate.

The four-point probe method was used to measure the electrical conductivity of the coatings deposited on alumina substrates by using Agilent 3458 A with four Pt aligned electrodes. The two outer probes act as current-carrying electrodes (I1, I2), while the two

inner ones are used to measure the voltages (E1, E2). The LNO/YSZ/LNO symmetric cells were used for EIS experiments through a Solartron 1260 impedance/gain-phase analyzer equipped with a furnace (Pekly, Thions Gardais, France) allowing temperatures from room temperature to 1000 °C under ambient air. One side of the symmetrical cell is in contact with a platinum plate, and the other side is placed with a platinum grid to ensure electrical contact. The EIS measurements were performed in the frequency range of 1 MHz–1 Hz with an amplitude voltage of 0.2 V under ambient air in the temperature range of 700–900 °C. The impedance spectra data were fitted by Z-View 3.5 software to extract impedance information.

3. Results and Discussion

3.1. Deposition of La–Ni–O Coatings

A transition of deposition mode (metallic mode ↔ oxide mode) occurs with the oxygen flow rate during the reactive deposition of oxide coatings by magnetron sputtering. Depending on the reactivity of the metal–metalloid system, the sputtering mode as a function of oxygen flow rate can be unstable, with the presence of a hysteresis loop. Figure 1 shows the discharge voltages of La and Ni targets as a function of oxygen flow rate under the applied discharge currents of 2.5 A and 0.5 A, respectively. Both curves present a hysteresis loop. For the lanthanum metallic target (Figure 1a), the target operates in the metallic mode up to an oxygen flow rate of 9 sccm, with a rather high deposition rate and a partial oxidation of the coating. A further increase in oxygen flow rate yields the drop of target voltage, which corresponds to the full target oxidation. Deposition in the so-called oxide mode with a sharp decrease in the deposition rate yields a fully oxidized coating. While decreasing oxygen flow rate, the target still operates in the oxide mode. When the oxygen flow rate continues to decrease between 2.0 and 2.5 sccm, the deposition mode returns to the metal mode. Likewise, a similar curve is observed on the Ni metallic target (Figure 1b) with a narrow unstable domain of the Ni–O system. With increasing oxygen flow rate, the metallic-to-oxide sputtering mode transition occurs between the oxygen flow rate of 1.5 and 2, while the opposite oxide-to-metallic transition appears between the oxygen flow rate of 1.5 and 2 by decreasing the oxygen flow rate from the oxide mode. Figure 2 shows the SEM cross-sections, deposition rate, and transmittance of three La–Ni–O coatings deposited under a rather high pressure of 2.4 Pa using an argon flow rate of 200 sccm. Oxygen flow rates were chosen in the metallic mode (oxygen flow rate of 1 sccm) and in the oxide mode (oxygen flow rate of 12 sccm) for both La and Ti targets. A third coating was deposited in the intermediate domain (oxygen flow rate of 6 sccm) of the hysteresis loop for the La target with a setpoint maintained in the oxide mode. From Figure 2a, the coating deposited under the metallic mode (oxygen flow rate of 1 sccm) presents a rather high deposition rate of 39.26 nm/min. As expected, the coating presents a metallic aspect with a strong light absorption (Figure 2d). The coating deposited under the oxide mode (oxygen flow rate of 12 sccm) presents a strong drop of the deposition rate (around 2.9 nm/min) conformal to the full oxidation of both La and Ni targets (Figure 2c). Its transmittance is weak at the wavelength up to about 600 nm and progressively increases with the wavelength to reach about 70% in the near-infrared domain at a 2500 nm wavelength (Figure 2d). The coating deposited under the oxygen flow rate of 6 sccm presents characteristics close to that of the coating deposited under the oxygen flow rate of 12 sccm: It has a higher deposition rate of around 6.3 nm/min (Figure 2b) and transmittance comparable to coatings deposited at the oxygen flow rate of 12 sccm (Figure 2d).

3.2. The Structure and Morphology Evolution of the La–Ni–O Coatings with the La/Ni Atomic Ratio of 2.04

Based on the above analysis, the La₂NiO₄ coatings were deposited in the intermediate domain, and the deposition parameters that allow a coating with a La/Ni atomic ratio of 2.04 are shown in Table 1. The coatings were deposited by co-sputtering of La and Ni

metallic targets under the mixed Ar/O₂ of 200/6 sccm. Previous work in our laboratory has shown that La₂NiO₄ coatings can be successfully synthesized by controlling the La/Ni atomic ratio close to 2 followed by suitable annealing treatment [20]. According to the Thornton’s diagram revised by Anders [22], the morphology of the coatings becomes less dense as the average energy of the impinging species decreases by increasing the deposition pressure. Previous works have shown that dense La₂NiO₄ coatings are deposited under a low pressure of 0.4 Pa [21]. The present work was carried out at a higher pressure of 2.4 Pa followed by an annealing treatment in order to obtain the appropriate porous coatings.

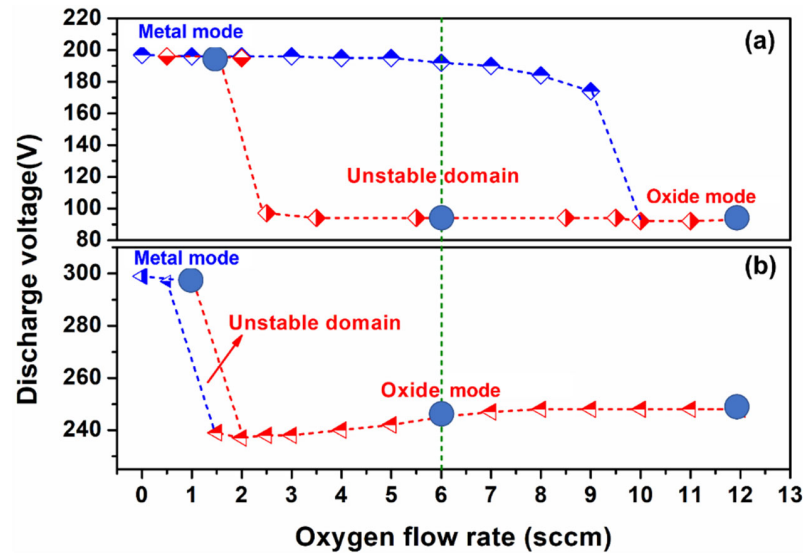


Figure 1. Hysteresis loop of the different targets under Ar flow of 200 sccm: (a) Applied 2.5 A on La target, (b) Applied 0.5 A on Ni.

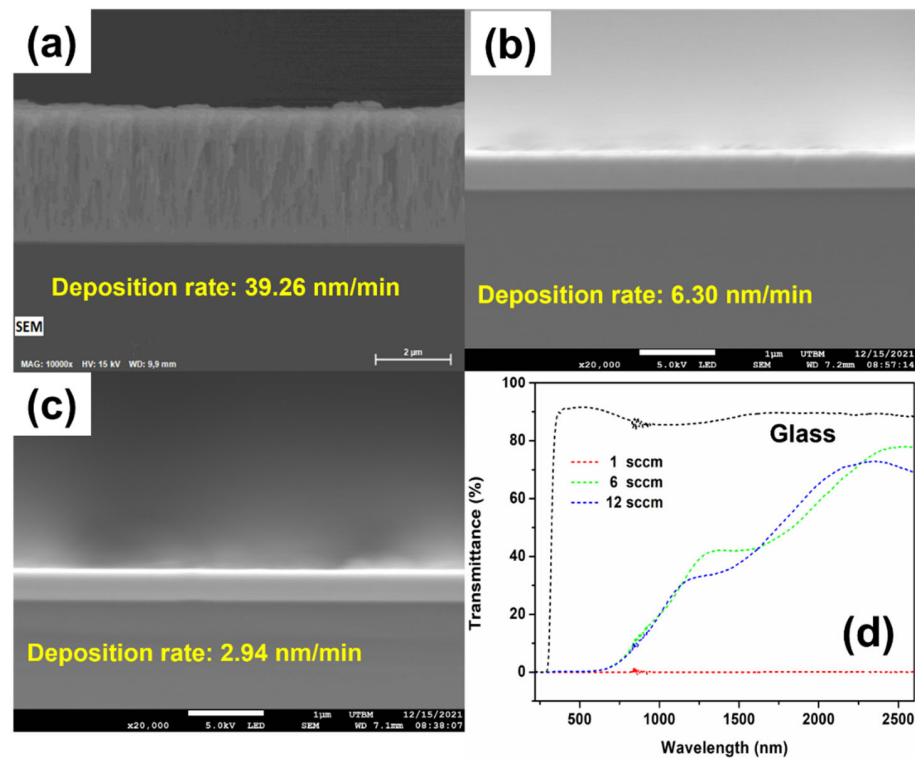
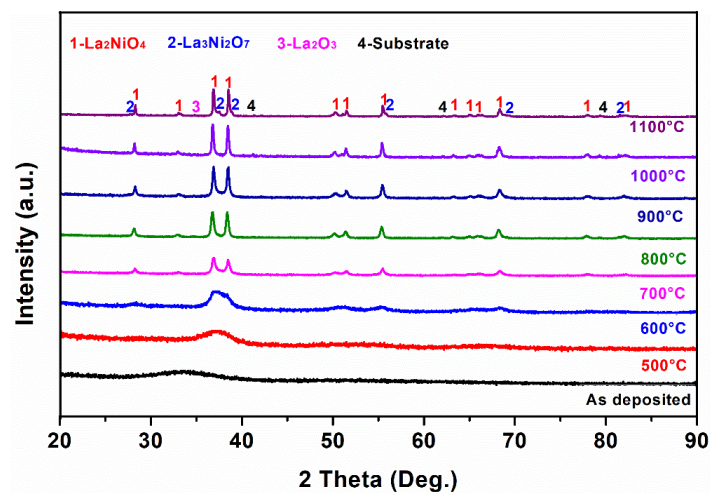


Figure 2. SEM cross-sections of La–Ni–O coatings deposited with 200 sccm Ar and (a) 1 sccm O₂, (b) 6 sccm O₂ with La target operating in the compound mode, (c) 12 sccm O₂. Optical transmission vs. wavelength of those three coatings (d).

Table 1. Sputtering parameters for deposition of La–Ni–O coatings with the La/Ni atomic ratio of 2.04.

Parameters	La Target	Ni Target
Ar flow rate (sccm)	200	200
O ₂ flow rate (sccm)	6	6
Total pressure (Pa)	2.4	2.4
Drawing distance (mm)	70	70
Power (W)	500	102
Frequency (kHz)	50	50
T _{off} (μs)	5	5

The as-deposited coatings were amorphous (Figure 3). Successive annealing treatments were realized under air for 2 h from 500 °C to 1100 °C, with steps of 100 °C, in order to obtain their crystallization. Annealing at 500 °C is characteristic of atomic rearrangements since the position of the maximum of the continuous background modulation shifts from about 34° to 38°. The coating starts to crystallize toward the La₂NiO₄ phase at 600 °C, while a relatively complete La₂NiO₄ phase appears at 700 °C. This can be judged from the appearance of two main peaks at 36.7° and 38.5° ascribed to the La₂NiO₄ phase. An ideal La₂NiO₄ coating with K₂NiF₄ structure can be obtained at 800 °C, which is consistent with the literature results [20]. Interestingly, a La₃Ni₂O₇ phase appeared after annealing at 1100 °C. This may promote the conductivity of the coatings due to the appearance of higher-order K_{n+1}Ni_nO_{3n+1} [23]. Additionally, the average grain size of the coating increases with the annealing temperature (Table 2). In particular, the average grain size increases sharply at 700 °C.

**Figure 3.** XRD measurements of La–Ni–O coatings with the La/Ni atomic ratio of 2.04 as function of annealing temperature for 2 h.**Table 2.** Average grain size of samples subjected to different annealing treatments.

Annealing Treatment	Average Grain Size (nm)
As deposited	1.9
500 °C for 2 h	3.7
600 °C for 2 h	5.1
700 °C for 2 h	27.0
800 °C for 2 h	32.0
900 °C for 2 h	36.2
1000 °C for 2 h	42.9
1100 °C for 2 h	71.2
1000 °C 2 h–750 °C 120 h	47.6

The morphological features of the coatings deposited on alumina plates were characterized by scanning electron microscopy with a backscattered electron detector (SEM-BED). Figures 4 and 5 shows the top surface and cross-section morphologies of the coatings as the annealing progresses. For the as-deposited coating, the morphology reproduces the alumina substrate roughness. Columnar growth was observed from the cross-section, which is consistent with the characteristics of general coatings deposited by magnetron sputtering. In addition, the coatings cover the substrate tightly and exhibit good adhesion. As the annealing temperature increased, the morphology of the coatings changed. The micro (or nano) pores began to appear in the coating near the alumina substrate at 700 °C with a whole volume that does not change much up to 900 °C (Figures 4d–f, 5d–f and 6). These pores should come from the elimination of intrinsic atomic-scale defects. At this time, the pores were not open, which was not conducive to oxygen diffusion. A porous morphology of a large size was observed on the top surface of the coating after annealing at 1000 °C (Figure 4g). Pores in the top surface of the coating after annealing at 1000 °C with a diameter between 20 and 120 nm occupy more than 90% (Figure 7a). As the annealing temperature increased to 1100 °C, the number of pores on the top surface of the coating decreased, but their size further increased (Figure 4h). The pore size of the coating after annealing at 1100 °C is concentrated mainly between 50 and 250 nm, accounting for more than 90% (Figure 7c). For the porous morphology, the cross-section of the coatings from 1000 °C to 1100 °C shows the same phenomenon as the top surface (Figures 4g–h and 7b,d). As the annealing temperature increases, the grain size increases, which in turn causes the micron (nano) pores to be aggregated into macropores accompanied by volume increase (Figure 6). Moreover, there are channels between the pores inside the coating, which is conducive to oxygen diffusion (Figure 4g,h). However, increasing the pore size reduces the number of small pores (from 1000 to 1100 °C), which may reduce the specific surface area inside the coating.

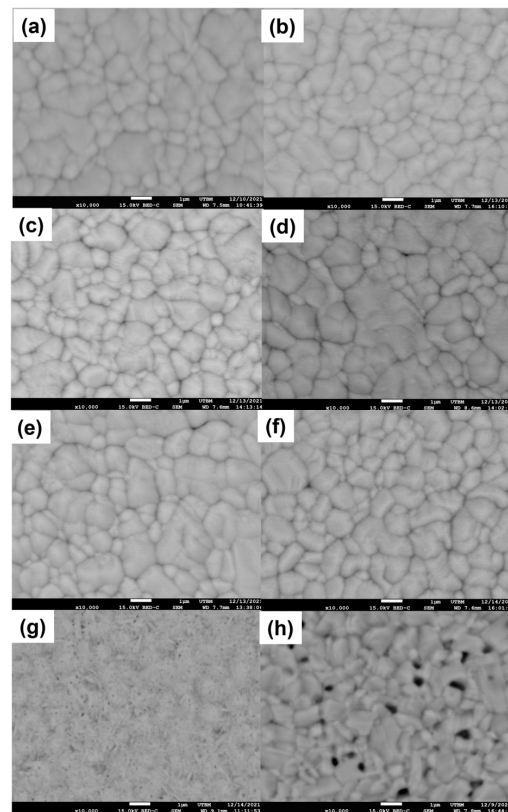


Figure 4. SEM-BED top views (a–h) of La–Ni–O coatings with the La/Ni atomic ratio of 2.04 deposited on alumina plates after annealing in air at different temperatures for 2 h: (a) as deposited, (b) 500 °C, (c) 600 °C, (d) 700 °C, (e) 800 °C, (f) 900 °C, (g) 1000 °C, and (h) 1100 °C.

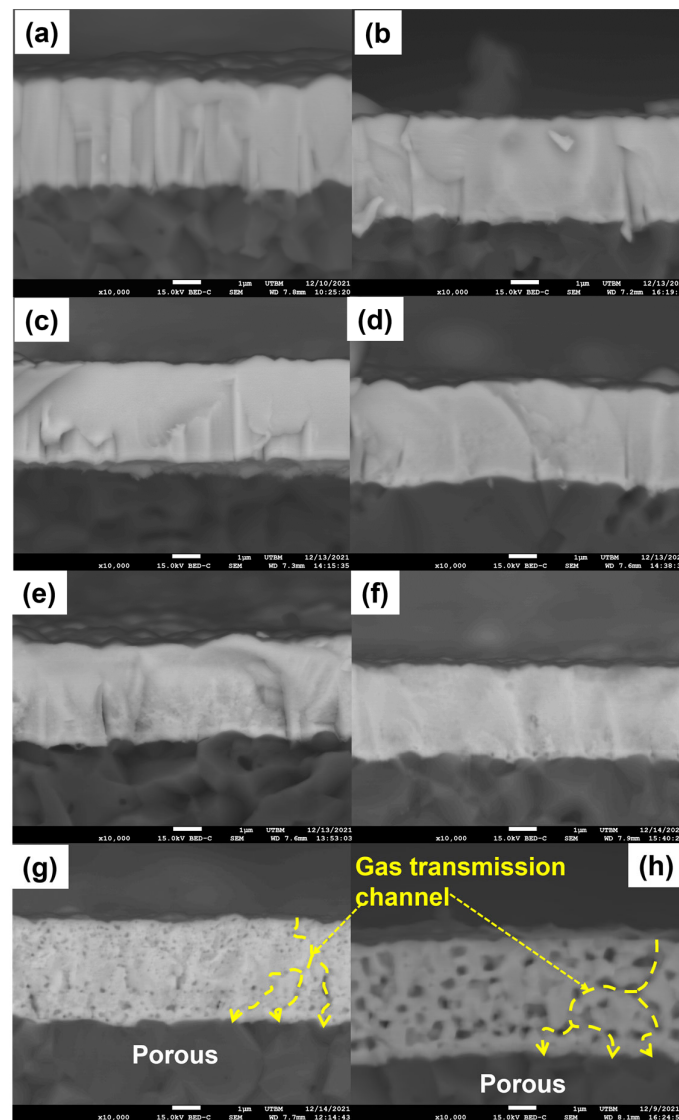


Figure 5. SEM-BED cross-sections (a–h) of La–Ni–O coatings with the La/Ni atomic ratio of 2.04 deposited on alumina plates after annealing in air at different temperatures for 2 h: (a) as deposited, (b) 500 °C, (c) 600 °C, (d) 700 °C, (e) 800 °C, (f) 900 °C, (g) 1000 °C, and (h) 1100 °C.

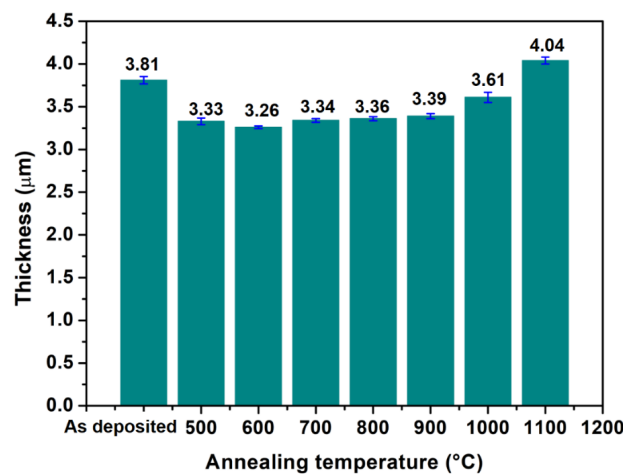


Figure 6. Thickness of the La–Ni–O coatings with the La/Ni atomic ratio of 2.04 deposited on alumina plate as a function of annealing temperature.

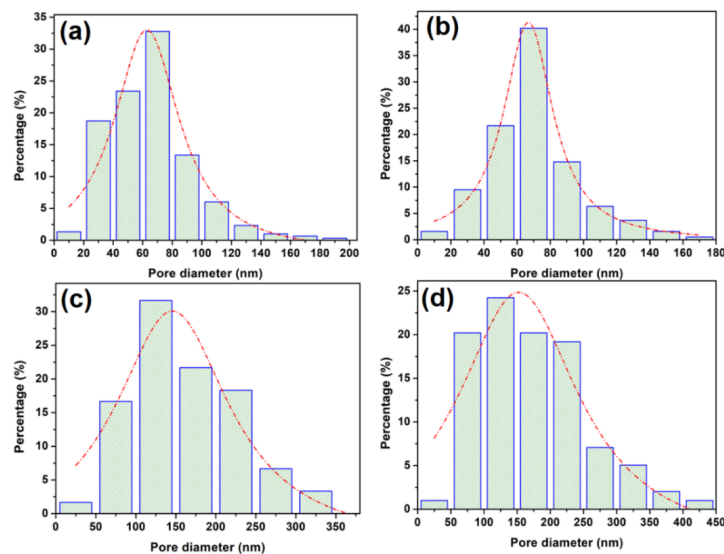


Figure 7. Pore size distribution of La–Ni–O coatings with La/Ni atomic ratio of 2.04: (a) top surface of after annealing at 1000 °C, (b) cross-section of after annealing at 1000 °C, (c) top surface of after annealing at 1100 °C, (d) cross-section of after annealing at 1100 °C.

A short-term stability experiment was performed to examine the stability of the coating. The coating deposited on the alumina plate after annealing at 1000 °C for 2 h was continuously annealing at 750 °C for 120 h. The structure and the porous morphology of the coating were assessed by XRD and SEM, respectively, as shown in Figures 8 and 9. The porous morphology of the coating was still well maintained (Figure 8a). Figure 8b shows that the number of the pores of the top surface in the larger pore size range (120–240 nm) was slightly increased compared to Figure 7a. However, the pore size distribution of the cross-section is still concentrated mainly in the 20–120 nm range. On the other hand, no obvious difference was observed in the cross-section (Figure 8c,d) of the coating compared to Figures 4g and 6b. This suggests that the porous morphology of the coating obtained after annealing at 1000 °C for 2 h remains relatively stable. The XRD result indicates the chemical stability of this coating at 750 °C (Figure 9), but the average grain size is increased (Table 2).

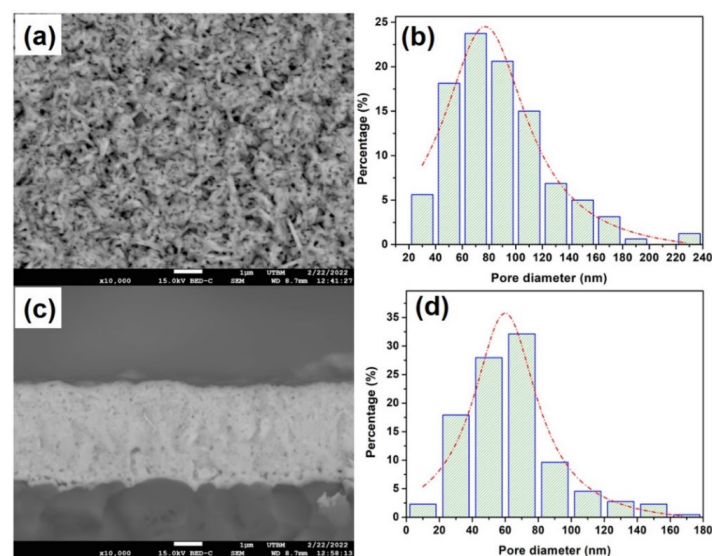


Figure 8. SEM-BED views and pore size distribution of La_2NiO_4 coatings after annealing in air at 1000 °C for 2 h followed by annealing at 750 °C in air for 120 h: SEM-BED view of top surface (a) and cross-section (c) and pore size distribution of top surface (b) and cross-section (d).

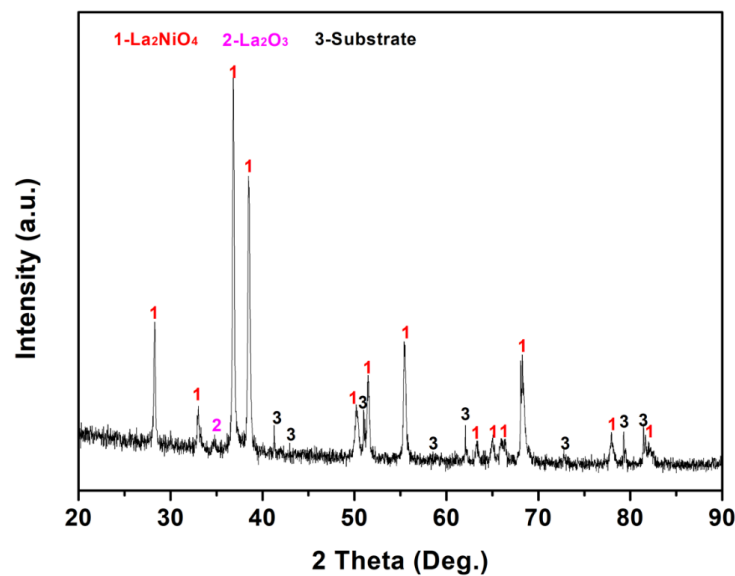


Figure 9. XRD measurements of La₂NiO₄ coatings after annealing at 1000 °C in air for 2 h followed by annealing at 750 °C in air for 120 h.

3.3. Electrical and Electrochemical Properties of the La₂NiO₄ Coatings

The coatings undergo crystallization, structure change, and morphology evolution during annealing treatments, which may affect their performance. In this work, the electrical conductivity of LNO coatings subjected to different annealing treatments and the electrochemical behavior of LNO/YSZ/LNO symmetric half-cells were assessed. The electrical conductivity of the LNO coatings deposited on alumina plates after different annealing treatments was analyzed by the four-point probe method under air (Figure 10). The electrical conductivity of LNO coatings undergoes three stages as a function of the annealing temperature. It first increases with the annealing temperature up to 700 °C, which may be attributed to the crystallization of the coatings. From 700 °C to 1000 °C, a decrease in electronic conductivity of the coating was observed, which may be affected by its increasing number of pores. The formation of higher-order phases (La₃Ni₂O₇) may be an important factor for the increase in the electronic conductivity observed from 1000 °C to 1100 °C [23]. Therefore, the electronic conductivity of the coating was affected by crystallization, phase nature, and morphology.

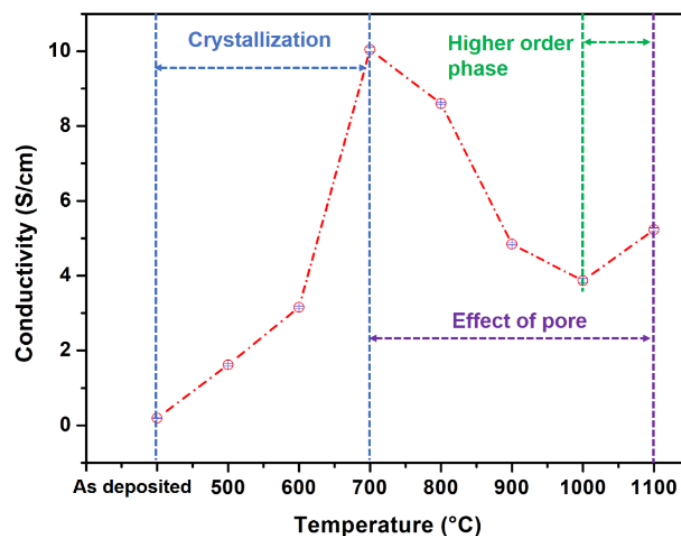


Figure 10. The conductivity of La–Ni–O coatings with La/Ni atomic ratio of 2.04 deposited on alumina substrate as function of annealing temperature for 2 h measured at room temperature.

To determine the electrochemical performances of the coatings as a function of the annealing temperature, coatings with thickness of 1.6 μm were deposited on both sides of the YSZ plates, named LNO–1 (annealing at 900 °C), LNO–2 (annealing at 1000 °C), and LNO–3 (annealing at 1100 °C), respectively. Electrochemical impedance spectroscopy (EIS) measurements of the LNO/YSZ/LNO symmetric half-cells were performed under air from 700 °C to 900 °C by steps of 50 °C. These EIS experiments were carried out with a voltage amplitude of 0.1 V in the frequency range from 10 MHz to 1 Hz with 11 points per decade. The impedance of all cells was normalized by multiplying the superficial area (0.1 cm²).

Nyquist plots of the symmetric half-cells obtained at 750 °C for LNO–1, LNO–2, and LNO–3 are shown in Figure 11. Three contributions are identified in the high, medium, and low frequency ranges. The contribution in medium and low frequency ranges can be explained as follows [24–26]: (i) the semicircle in the medium frequency range (MF) was attributed to the transfer of O^{2–} from the electrode to the electrolyte; and (ii) the large depress arc in low frequency range (LF) represents an oxygen adsorption/dissociation step overlapping with the diffusion process. Generally, high frequency resistance (R_s) was attributed to electrolyte resistance. To facilitate analysis of the LNO cathode, R_s was removed. The contributions appearing in MF and LF ranges corresponding to that of the LNO electrode were fitted by an equivalent circuit consisting of two Resistance–Constant Phase Elements (R–CPE) in parallel, associated in series (see Figure 11).

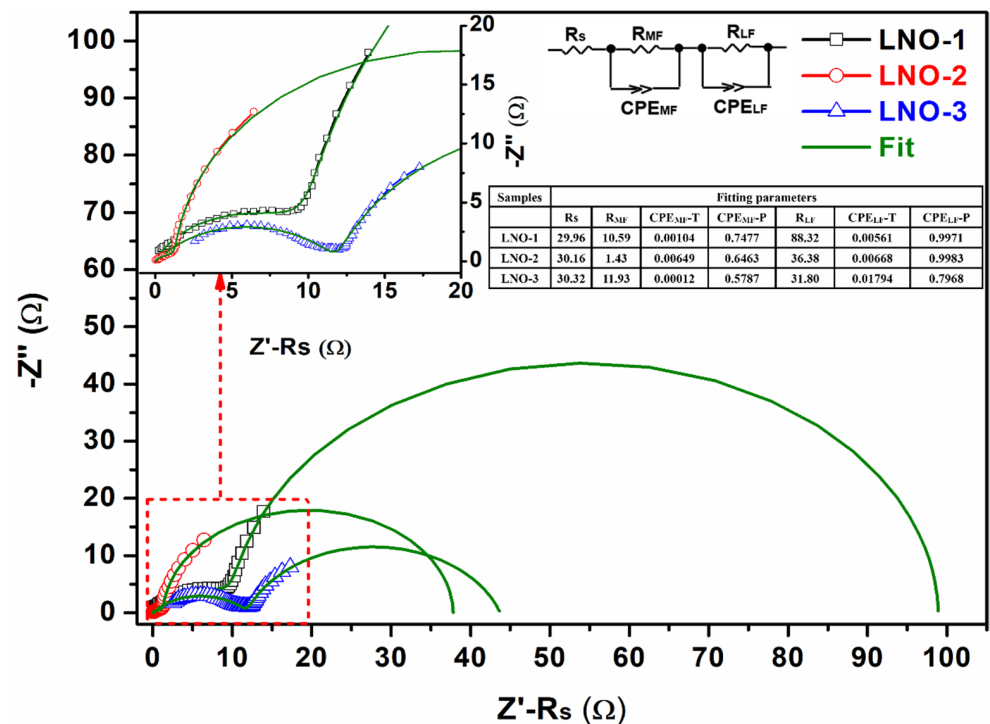


Figure 11. Nyquist plots of LNO symmetrical cells deposited on YSZ electrolyte at 750 °C: LNO–1 after annealing at 900 °C for 2 h, LNO–2 after annealing at 1000 °C for 2 h, LNO–3 after annealing at 1100 °C for 2 h.

The Nyquist plots were fitted by Z-View software, where the open symbols represent the experimental measurements, and the green lines represent the fitting results. Relevant resistance and capacitance information were extracted from the fitting results to calculate polarization resistance, activation energy, and equivalent capacitance. The polarization resistance was calculated by the Formula (1):

$$R_p = \left(\frac{(R_{MF} + R_{LF}) \times S}{2} \right) \tag{1}$$

where R_{MF} and R_{LF} were the resistance values at the MF and LF ranges, respectively, and S is the superficial area (0.1 cm^2).

The activation energy (E_a) for electrochemical behavior was calculated according to the Arrhenius relation from the slope of the curve $\ln R = f(1000/T)$. The equivalent capacitance (C_{eq}) was calculated using Formula (2):

$$C_{eq} = R e^{\frac{1-n}{n}} \times CPE^{\frac{1}{n}} \tag{2}$$

where R was the electrical resistance, n , the decentering parameter of the Constant Phase Element, and CPE , the capacitance of the Constant Phase Element.

Figure 12 presents the R_p calculated from EIS measurements from $700 \text{ }^\circ\text{C}$ to $900 \text{ }^\circ\text{C}$ for LNO-1, LNO-2, and LNO-3. The R_p of all the samples decreased with increasing temperature. LNO-2 and LNO-3 exhibit lower R_p than LNO-1, which may be attributed to the porous morphology if we refer to previous work [9]. At an intermediate temperature ($700 \text{ }^\circ\text{C}$), the R_p of LNO-2 is $2.37 \text{ } \Omega \cdot \text{cm}^2$, which is in agreement with the $4.0 \text{ } \Omega \cdot \text{cm}^2$ of Zhao et al. [27], the $7.77 \text{ } \Omega \cdot \text{cm}^2$ of Escudero et al. [28], and the $2.1 \text{ } \Omega \cdot \text{cm}^2$ of Benamira et al. [29]. For the activation energy of electrochemical phenomena, LNO-2 shows the lowest value of 0.44 eV compared to LNO-1 and LNO-3, which is close to the previous work of 0.4 eV and lower than the values of the literature (Table 3).

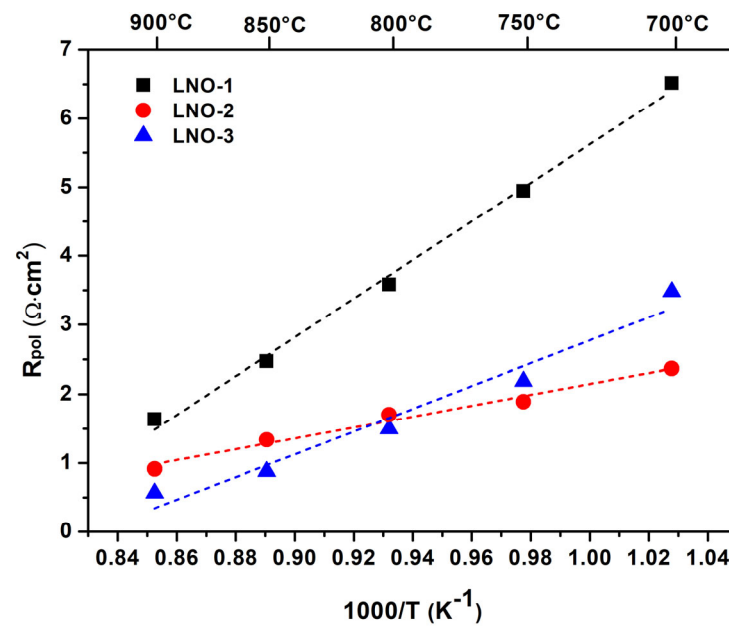


Figure 12. The Arrhenius curves of polarization resistance (R_{pol}) for LNO-1, LNO-2, and LNO-3 from $700 \text{ }^\circ\text{C}$ to $900 \text{ }^\circ\text{C}$.

Table 3. The activation energy of LNO-1, LNO-2, and LNO-3.

Samples	E_a Calculated from R_{pol} (eV)
LNO-1	0.67
LNO-2	0.44
LNO-3	0.89
LNO	1.47 [25], 1.2 [26], 1.0 [28], 0.4 [9]

Furthermore, Figures 13 and 14 present the Arrhenius plots of R_p and equivalent capacitances at the MF and LF ranges, corresponding to different electrochemical responses. It can be seen from Figure 13 that LNO-1 has the highest R_p in the LF range, which may be limited by the O_2 diffusion caused by the closed micro (nano) pore morphology. Similarly, LNO-3 exhibits the lowest R_p in the LF range, thanks to the porous morphology with a

larger pore size. LNO-2 has a clear advantage in the MF range compared to LNO-1 and LNO-3, which may be the result of a combination of two reasons: (i) the abundant porous morphology promotes the diffusion of O₂; and (ii) more specific surface area provides more oxygen adsorption sites and thus enhances the ORR. From Figure 14, the equivalent capacitance in the MF range was much lower than that in the LF range for LNO-1, LNO-2, and LNO-3, which was consistent with the study by Mauvy et al. [24]. In general, low capacitance was thought to be associated with ion transport, gas adsorption/desorption, and ORR [9,30,31]. The equivalent capacitance of LNO-2 was between LNO-1 and LNO-3 in the MF range, which may also verify that LNO-2 has the lowest R_p in the MF range due to the combined effect of the two reasons mentioned above.

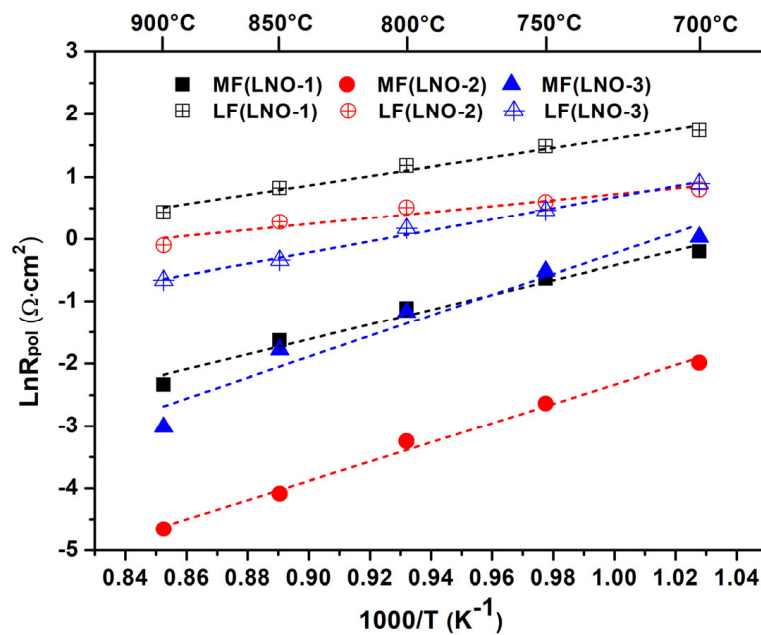


Figure 13. The Arrhenius curves of polarization resistance (R_{pol}) in the medium and low frequency range of LNO-1, LNO-2, and LNO-3 from 700 °C to 900 °C.

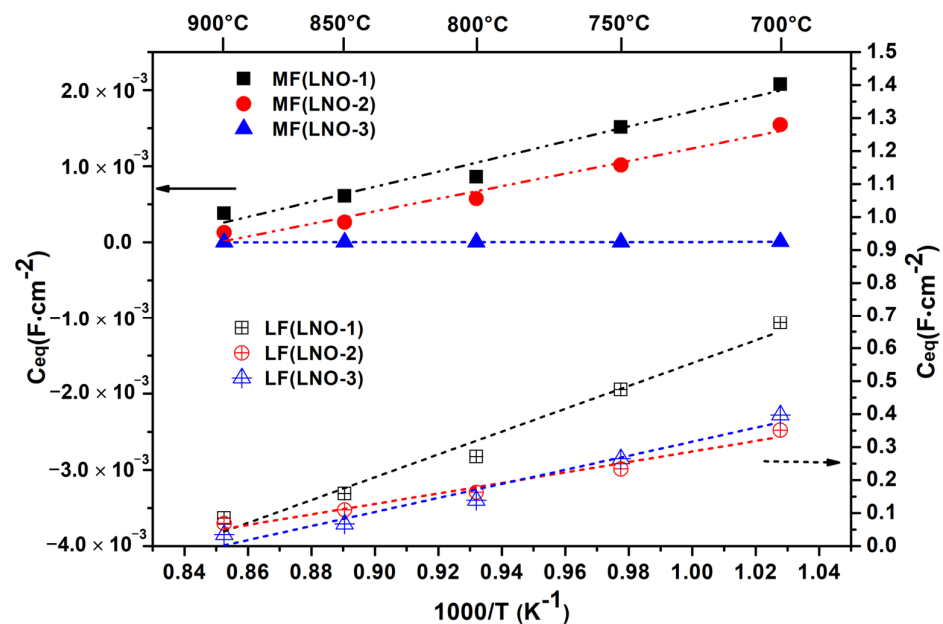


Figure 14. The Arrhenius curves of the equivalent capacities calculated from the fitting values in the medium and low frequency range of LNO-1, LNO-2, and LNO-3 from 700 °C to 900 °C.

4. Conclusions

The La–Ni–O coating with a La/Ni atomic ratio of about 2.04 deposited by reactive magnetron sputtering was subjected to a suitable annealing treatment process to obtain a porous LNO coating with a La_2NiO_4 phase. The annealing temperature was crucial to the formation of the La_2NiO_4 phase and the porous morphology. The LNO coating with abundant pores was obtained after annealing at 1000 °C for 2 h. Electrochemical impedance spectroscopy (EIS) characterization of the symmetrical cells indicated that the LNO–2 cathode obtained by annealing at 1000 °C exhibited lower polarization resistance compared to the LNO–1 (annealing at 900 °C) and LNO–3 (annealing at 1100 °C) cathodes. The short-term stability experiment confirmed the stability of this porous morphology at the operating temperature of 750 °C. This work aims to provide a reference for the direct synthesis of appropriate porous LNO cathodes on electrolyte by magnetron sputtering. Nevertheless, further works must be carried out, such as lowering the subsequent annealing temperature to facilitate more flexible applications in the fabrication of metal-supported solid oxide fuel cells (MS-SOFC) operating at intermediate temperatures.

Author Contributions: Conceptualization, H.L.; Data curation, X.Y.; Formal analysis, M.H.; Investigation, X.Y.; Methodology, X.Y.; Resources, P.B. (Pascal Briois); Visualization, H.L. and P.B. (Pierre Bertrand); Writing—original draft, X.Y.; Writing—review & editing, P.B. (Pascal Briois), H.L., A.B. and P.B. (Pierre Bertrand). All authors have read and agreed to the published version of the manuscript.

Funding: This research was funded by China Scholarship Council (No. 201808530576) and Natural Science Basic Research Plan in Shaanxi Province of China (2022JQ-551).

Institutional Review Board Statement: Not applicable.

Informed Consent Statement: Not applicable.

Data Availability Statement: Not applicable.

Acknowledgments: The authors thank the China Scholarship Council, Natural Science Basic Research Plan in Shaanxi Province of China, and Pays de Montbéliard Agglomeration for their financial support of this work.

Conflicts of Interest: The authors declare no conflict of interest.

References

1. Vohs, J.M.; Gorte, R.J. High-performance SOFC cathodes prepared by infiltration. *Adv. Mater.* **2009**, *21*, 943–956. [[CrossRef](#)]
2. Yang, L.; Wang, S.; Blinn, K.; Liu, M.; Liu, Z.; Cheng, Z.; Liu, M. Enhanced sulfur and coking tolerance of a mixed ion conductor for SOFCs: $\text{BaZr}_{0.1}\text{Ce}_{0.7}\text{Y}_{0.2-x}\text{Yb}_x\text{O}_{3-\delta}$. *Science* **2009**, *326*, 126–129. [[CrossRef](#)] [[PubMed](#)]
3. Li, M.; Zhao, M.; Li, F.; Zhou, W.; Peterson, V.K.; Xu, X.; Shao, Z.; Gentle, I.; Zhu, Z. A niobium and tantalum co-doped perovskite cathode for solid oxide fuel cells operating below 500 °C. *Nat. Commun.* **2017**, *8*, 13990. [[CrossRef](#)] [[PubMed](#)]
4. Chen, Y.; Choi, Y.; Yoo, S.; Ding, Y.; Yan, R.; Pei, K.; Qu, C.; Zhang, L.; Chang, I.; Zhao, B.; et al. A highly efficient multi-phase catalyst dramatically enhances the rate of oxygen reduction. *Joule* **2018**, *2*, 938–949. [[CrossRef](#)]
5. Alenazey, F.; Alyousef, Y.; AlOtaibi, B.; Almutairi, G.; Minakshi, M.; Cheng, C.K.; Vo, D.V.N. Degradation behaviors of solid oxide fuel cell stacks in steady-state and cycling conditions. *Energy Fuels* **2020**, *34*, 14864–14873. [[CrossRef](#)]
6. DiGiuseppe, G.; Sun, L. Electrochemical performance of a solid oxide fuel cell with an LSCF cathode under different oxygen concentrations. *Int. J. Hydrogen Energy* **2011**, *36*, 5076–5087. [[CrossRef](#)]
7. Zhang, Y.; Chen, B.; Guan, D.; Xu, M.; Ran, R.; Ni, M.; Zhou, W.; O'hayre, R.; Shao, Z. Thermal-expansion offset for high-performance fuel cell cathodes. *Nature* **2021**, *591*, 246–251. [[CrossRef](#)]
8. Xu, K.; Pei, K.; Zhao, B.; Zhao, Y.; Niu, Q.; Chen, Y. An oxygen reduction reaction active and durable SOFC cathode/electrolyte interface achieved via a cost-effective spray-coating. *Int. J. Hydrogen Energy* **2021**, *46*, 32242–32249. [[CrossRef](#)]
9. Dailly, J.; Fourcade, S.; Largeteau, A.; Mauvy, F.; Grenier, J.C.; Marrony, M. Perovskite and A_2MO_4 -type oxides as new cathode materials for protonic solid oxide fuel cells. *Electrochim. Acta* **2010**, *55*, 5847–5853. [[CrossRef](#)]
10. Burriel, M.; Santiso, J.; Rossell, M.D.; Tendeloo, G.V.; Figueras, A.; Garcia, G. Enhancing total conductivity of $\text{La}_2\text{NiO}_{4+\delta}$ epitaxial thin films by reducing thickness. *J. Phys. Chem. C* **2008**, *112*, 10982–10987. [[CrossRef](#)]
11. Flura, A.; Dru, S.; Nicolle, C.; Vibhu, V.; Fourcade, S.; Lebraud, E.; Rougier, A.; Bassat, J.-M.; Grenier, J.-C. Chemical and structural changes in $\text{Ln}_2\text{NiO}_{4+\delta}$ (Ln = La, Pr or Nd) lanthanide nickelates as a function of oxygen partial pressure at high temperature. *J. Solid State Chem.* **2015**, *228*, 189–198. [[CrossRef](#)]

12. Fondard, J.; Billard, A.; Bertrand, G.; Briois, P. $\text{Ln}_2\text{NiO}_{4+\delta}$ (Ln = La, Pr, Nd) coatings deposited by reactive magnetron sputtering as cathode material for intermediate temperature solid oxide fuel cell. *Vacuum* **2018**, *152*, 97–108. [[CrossRef](#)]
13. Wu, J.; Liu, X. Recent development of SOFC metallic interconnect. *J. Mater. Sci. Technol.* **2010**, *26*, 293–305. [[CrossRef](#)]
14. Zhao, K.; Wang, Y.P.; Chen, M.; Xu, Q.; Kim, B.H.; Huang, D.P. Electrochemical evaluation of $\text{La}_2\text{NiO}_{4+\delta}$ as a cathode material for intermediate temperature solid oxide fuel cells. *Int. J. Hydrogen Energy* **2014**, *39*, 7120–7130. [[CrossRef](#)]
15. Philippeau, B.; Mauvy, F.; Mazataud, C.; Fourcade, S.; Grenier, J.C. Comparative study of electrochemical properties of mixed conducting $\text{Ln}_2\text{NiO}_{4+\delta}$ (Ln = La, Pr and Nd) and $\text{La}_{0.6}\text{Sr}_{0.4}\text{Fe}_{0.8}\text{Co}_{0.2}\text{O}_{3-\delta}$ as SOFC cathodes associated to $\text{Ce}_{0.9}\text{Gd}_{0.1}\text{O}_{2-\delta}$, $\text{La}_{0.8}\text{Sr}_{0.2}\text{Ga}_{0.8}\text{Mg}_{0.2}\text{O}_{3-\delta}$ and $\text{La}_9\text{Sr}_1\text{Si}_6\text{O}_{26.5}$ electrolytes. *Solid State Ion.* **2013**, *249*, 17–25. [[CrossRef](#)]
16. Yang, S.H.; Kim, K.H.; Yoon, H.H.; Kim, W.J.; Choi, H.W. Comparison of combustion and solid-state reaction methods for the fabrication of SOFC LSM cathodes. *Mol. Cryst. Liq. Cryst.* **2011**, *539*, 50–390. [[CrossRef](#)]
17. Solovyev, A.; Burmistrov, I.N.; Rabotkin, S.; Shipilova, A.; Yalovenko, D.V.; Semenov, V.; Bredikhin, S.I. Electrochemical Characterization of Intermediate-Temperature Solid Oxide Fuel Cells with PVD-Coated Electrolyte. *ECS Trans.* **2021**, *103*, 105. [[CrossRef](#)]
18. Gannon, P.; Deibert, M.; White, P.; Smith, R.; Chen, H.; Priyantha, W.; Gorokhovskiy, V. Advanced PVD protective coatings for SOFC interconnects. *Int. J. Hydrogen Energy* **2008**, *33*, 3991–4000. [[CrossRef](#)]
19. Jung, W.; Kim, J.J.; Tuller, H.L. Investigation of nanoporous platinum thin films fabricated by reactive sputtering: Application as micro-SOFC electrode. *J. Power Source* **2015**, *275*, 860–865. [[CrossRef](#)]
20. Briois, P.; Perry, F.; Billard, A. Structural and electrical characterisation of lanthanum nickelate reactively sputter-deposited thin films. *Thin Solid Films* **2008**, *516*, 3282–3286. [[CrossRef](#)]
21. Fondard, J.; Billard, A.; Bertrand, G.; Briois, P. Synthesis and characterization of $\text{La}_2\text{NiO}_{4+\delta}$ coatings deposited by reactive magnetron sputtering using plasma emission monitoring. *Solid State Ion.* **2014**, *265*, 73–79. [[CrossRef](#)]
22. Anders, A.X. A structure zone diagram including plasma-based deposition and ion etching. *Thin Solid Films* **2010**, *518*, 4087–4090. [[CrossRef](#)]
23. Amow, G.; Davidson, I.J.; Skinner, S.J. A comparative study of the Ruddlesden-Popper series, $\text{La}_{n+1}\text{Ni}_n\text{O}_{3n+1}$ (n = 1, 2 and 3), for solid-oxide fuel-cell cathode applications. *Solid State Ion.* **2006**, *177*, 1205–1210. [[CrossRef](#)]
24. Mauvy, F.; Lalanne, C.; Bassat, J.M.; Grenier, J.C.; Zhao, H.; Huo, L.; Stevens, P. Electrode properties of $\text{Ln}_2\text{NiO}_{4+\delta}$ (Ln = La, Nd, Pr): AC impedance and DC polarization studies. *J. Electrochem. Soc.* **2006**, *153*, A1547. [[CrossRef](#)]
25. Minakshi, M.; Mitchell, D.R.; Munnangi, A.R.; Barlow, A.J.; Fichtner, M. New insights into the electrochemistry of magnesium molybdate hierarchical architectures for high performance sodium devices. *Nanoscale* **2018**, *10*, 13277–13288. [[CrossRef](#)] [[PubMed](#)]
26. Barmi, M.J.; Minakshi, M. Tuning the redox properties of the nanostructured CoMoO_4 electrode: Effects of surfactant content and synthesis temperature. *ChemPlusChem* **2016**, *81*, 964–977. [[CrossRef](#)]
27. Zhao, H.; Mauvy, F.; Lalanne, C.; Bassat, J.M.; Fourcade, S.; Grenier, J.C. New cathode materials for ITSOFC: Phase stability, oxygen exchange and cathode properties of $\text{La}_{2-x}\text{NiO}_{4+\delta}$. *Solid State Ion.* **2008**, *179*, 2000–2005. [[CrossRef](#)]
28. Escudero, M.J.; Aguadero, A.; Alonso, J.A.; Daza, L. A kinetic study of oxygen reduction reaction on La_2NiO_4 cathodes by means of impedance spectroscopy. *J. Electroanal. Chem.* **2007**, *611*, 107–116. [[CrossRef](#)]
29. Benamira, M.; Ringuedé, A.; Cassir, M.; Horwat, D.; Lenormand, P.; Ansart, F.; Bassat, J.M.; Viricelle, J.P. Enhancing oxygen reduction reaction of YSZ/ $\text{La}_2\text{NiO}_{4+\delta}$ using an ultrathin $\text{La}_2\text{NiO}_{4+\delta}$ interfacial layer. *J. Alloys Compd.* **2018**, *746*, 413–420. [[CrossRef](#)]
30. Garbayo, I.; Esposito, V.; Sanna, S.; Morata, A.; Pla, D.; Fonseca, L.; Sabaté, N.; Tarancón, A. Porous $\text{La}_{0.6}\text{Sr}_{0.4}\text{CoO}_{3-\delta}$ thin film cathodes for large area micro solid oxide fuel cell power generators. *J. Power Source* **2014**, *248*, 1042–1049. [[CrossRef](#)]
31. Boukamp, B.A.; Hildenbrand, N.; Nammensma, P.; Blank, D.H. The impedance of thin dense oxide cathodes. *Solid State Ion.* **2011**, *192*, 404–408. [[CrossRef](#)]

Disclaimer/Publisher’s Note: The statements, opinions and data contained in all publications are solely those of the individual author(s) and contributor(s) and not of MDPI and/or the editor(s). MDPI and/or the editor(s) disclaim responsibility for any injury to people or property resulting from any ideas, methods, instructions or products referred to in the content.